Using Fourier-Plane Imaging Microscopy for Determining Transition-Dipole-Moment Orientations in Organic Light-Emitting Devices

Jongchan Kim,[1] Haonan Zhao,[2] Shaocong Hou,[1] Mandeep Khatoniar,[3,4] Vinod Menon,[3,4] and Stephen R. Forrest[1,2,5,*]

[1] *Department of Electrical and Computer Engineering, University of Michigan, Ann Arbor, Michigan, USA*
[2] *Department of Physics, University of Michigan, Ann Arbor, Michigan, USA*
[3] *Department of Physics, City College, City University of New York, New York 10031, USA*
[4] *Department of Physics, Graduate Center, City University of New York, New York 10016, USA*
[5] *Department of Materials Science and Engineering, University of Michigan, Ann Arbor, Michigan, USA*

(Received 13 July 2020; revised 12 August 2020; accepted 19 August 2020; published 17 September 2020)

We use Fourier-plane imaging microscopy (FIM) to determine the transition-dipole-moment orientation in doped organic emissive thin films. The use of FIM enables precise, sensitive, and rapid measurement of dipole orientation in the emission layer of an organic light-emitting device (OLED). An optical model of a stratified birefringent multilayer is introduced for interpreting results obtained by FIM. Using the model, we determine the average orientation of transition-dipole-moment vectors of three phosphorescent dopant emitters. The dipole alignment measured by FIM quantitatively explains the difference in OLED efficiencies using these archetype dopant molecules. FIM provides a nondestructive tool to measure and ultimately improve the outcoupling efficiency of OLEDs and other light-emitting devices.

DOI: 10.1103/PhysRevApplied.14.034048

I. INTRODUCTION

The orientation of molecules affects various aspects of an organic film [1–3]. For example, the orientation of doped emitting molecules can affect the light outcoupling efficiency of organic light-emitting devices (OLEDs) [4,5]. That is, emitting molecules whose transition dipole moments (TDMs) are aligned parallel to the substrate plane increase coupling into optical modes within the viewing direction compared to moments oriented perpendicular to the substrate. The TDM orientation is also correlated with the radiative lifetime of excitons in an optical cavity due to the Purcell effect, which can affect processes such as exciton and polaron annihilation at high intensities.

A number of methods have been proposed to reveal the orientation of molecules within organic thin films, although many entail complex experimental setups and may lack the sensitivity required for a given application [6–11]. Recently, Fourier-plane imaging microscopy (FIM), which is a class of fluorescence microscopy measuring the angular emission intensity distribution from a film, has been used to identify the orientation of the emissive TDM in various materials [12–22]. In FIM, a large proportion of the light emitted into the substrate is simultaneously collected by the objective lens, and imaged by a 2D charge coupled device (CCD), resulting in a dramatically reduced measurement time and improved precision compared to conventional 1D scanning methods [9]. In this work, we use FIM to determine the TDM orientation for different luminescent dopants used in an OLED light-emitting layer. This information is useful in understanding, and improving the device outcoupling efficiency. We present an optical model to interpret the FIM polar images following the dyadic Green's function method in cylindrical coordinates that is based on the dipole model of Chance, Prock, and Silbey (CPS) [23]. The method determines the Poynting vector within a birefringent medium, from which we obtain the angular intensity distribution that reveals the TDM orientation. The dipole model is an extension of previous work [24] that includes consideration of birefringent media commonly used in organic electronic structures. The cylindrically symmetric solution is compact, and enables straightforward application to stratified birefringent multilayers. We validate our model by measuring the orientation of three emissive dopants, namely *fac*-tris(2-phenylpyridine)iridium(III) ($Irppy_3$), bis[2-(2-pyridinyl-N)phenyl-C](acetylacetonate)iridium(III) ($Irppy_2acac$), and monoamido-aminocarbene Cu carbazole [(MAC)CuCz] doped in 4,4′-bis(N-carbazolyl)-1,1′-biphenyl (CBP), and compare the FIM data with the outcoupling efficiency from the OLEDs incorporating these same emissive layers.

*stevefor@umich.edu

 © 2020 American Physical Society

II. THEORY

Light emitted from a dopant molecule has a dipole radiation pattern shown in Fig. 1(a), allowing for identifying its orientation from its angular emission profile. The analysis is done by decomposing the light intensity from different directions, characterized by the in-plane wave vector, $\kappa = k_0 \cdot n \cdot \sin\theta$, where k_0 is the wave vector in free space, n is the refractive index of the medium, and θ is the angle between the substrate normal and the propagation direction.

Fraunhofer and Fresnel approximations are used for analyzing diffraction patterns at different distances from the source to the image plane. The Fraunhofer approximation simplifies the calculations due to the suppressed phase factor; however, it can only be applied at large distances from the source [25]. The Fraunhofer approximation can be used at small distances, however, by placing a Fourier lens between the source and the image plane that transforms a parabolic wave in the near field into a plane wave. Fourier-plane imaging, also known as back-focal-plane imaging,

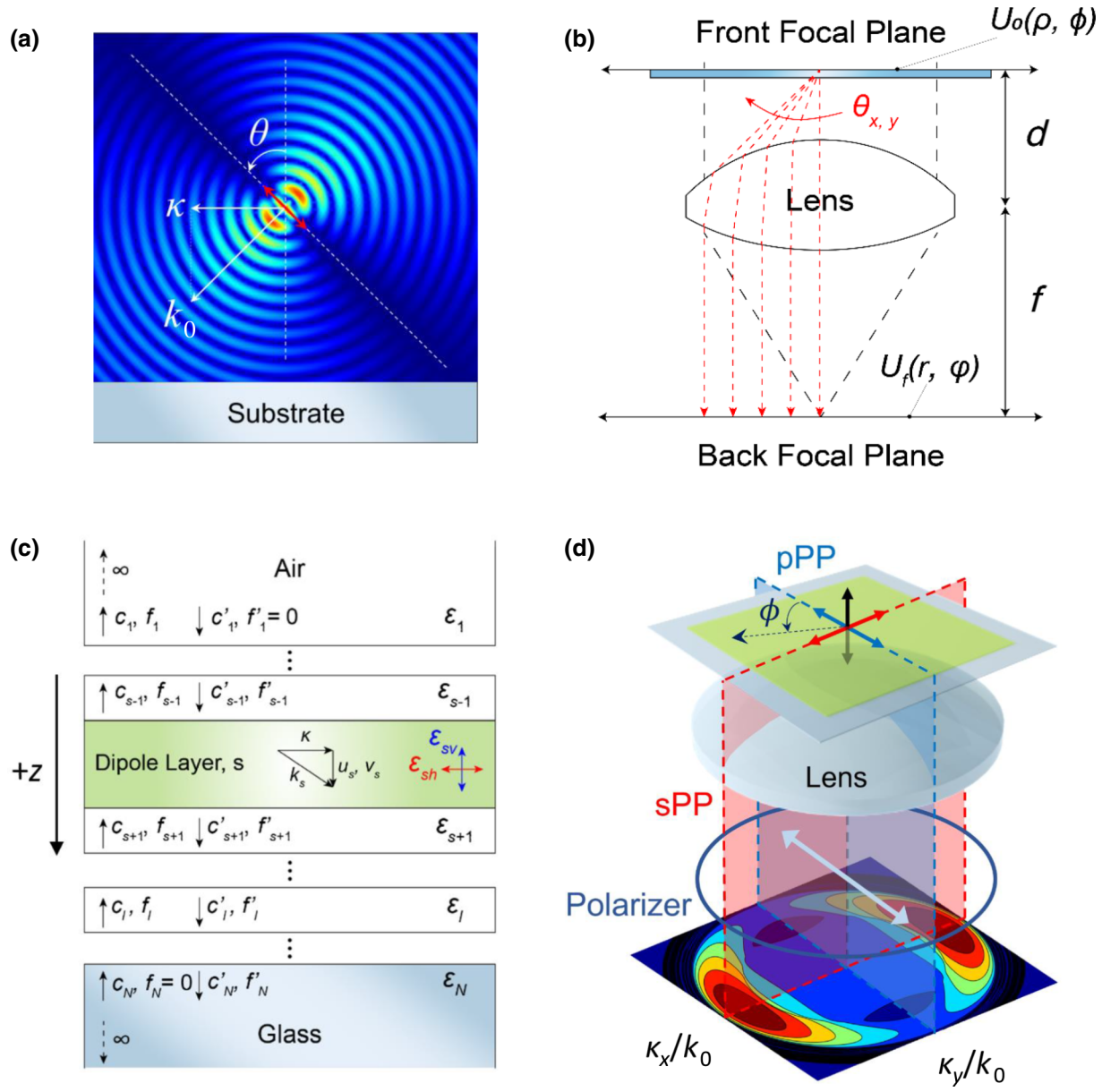

FIG. 1. Illustrations for understanding Fourier-plane imaging microscopy. (a) Calculated electric field of an oscillating dipole whose transition dipole moment is at angle θ relative to the substrate normal. The wave vector, k_0, and its in-plane component, κ, are shown. (b) Geometries for the Fourier transform operation of a Fourier lens. (c) A stratified multilayer structure used for the optical calculation defining the various wave vectors (κ, k, u, v), coefficients of the traveling wave eigenfunctions (c, f), and dielectric components (ε) in each layer. The subscripts s and l denote the source and arbitrary layer within the multilayer, respectively. (d) A schematic showing how a FIM polar plot is obtained from a point dipole. The two orthogonal planes, sPP and pPP, are defined by the linear polarizer.

decomposes an image into the weighted sum of its plane wave components. Placing the source in the front focal plane of a Fourier lens as in Fig. 1(b) results in a Fraunhofer diffraction pattern of the input field in the back focal plane described by [25]

$$U_f(r,\varphi) = \frac{\exp\left[i\frac{k}{2f}\left(1-\frac{d}{f}\right)r^2\right]}{i\lambda f} \times \int_0^{2\pi}\int_0^{\infty} U_0(\rho,\phi)\exp\left[-i\frac{2\pi}{\lambda f}\{\rho r\cos(\phi-\varphi)\}\right] \times \rho d\rho d\phi = m(r)\cdot F_0(k_\rho,\varphi), \quad (1)$$

where ρ, ϕ and r, φ are the polar coordinates of the front and back focal planes, respectively. $U_0(\rho, \phi)$ and $U_f(r, \varphi)$ are the input and output intensity distributions, respectively, f is the lens focal length, d is the propagation distance, λ is the wavelength, $F_0(k_\rho, \varphi)$ is the Fourier transform of the input function, $U_0(\rho, \phi)$, and k_ρ $(=\kappa/k_0)$ is the normalized in-plane wave vector in the front focal plane with $k_\rho = 1/2\pi\ k_0 \sin\theta_x \approx r/\lambda f$ for paraxial plane waves when $\phi = \varphi$. Note that $U_f(r, \varphi)$ is a Fourier transform of the input function in k-space, with a quadratic phase factor, $m(r)$. Here, $m(r)$ is a complex number for $d \geq f$. Thus, the phase curvature disappears for the sample plane at $d = f$, resulting in an output function in the back focal plane of the Fourier transform of $U_0(\rho, \phi)$.

In Eq. (1), $F_0(k_\rho, \varphi)$ corresponds to the far-field angular profile of a point dipole. Here, we follow the formulation of the CPS model [23] and previous work [24] to derive F_0 in a birefringent medium using dyadic Green's functions for the multilayer reference structure in Fig. 1(c). The use of a dyadic Green's function assumes cylindrical symmetry of emission from a dipole source. This enables a compact solution compared to previous scattering matrix methods [26,27]. The dipole source at the origin, $\boldsymbol{\xi}' = (0, 0, 0)$, is embedded in the sth layer, with either a vertical or horizontal orientation. We assume all layers are uniaxial with a complex dielectric tensor, ε_l:

$$\varepsilon_l = \begin{pmatrix} \varepsilon_{lh} & 0 & 0 \\ 0 & \varepsilon_{lh} & 0 \\ 0 & 0 & \varepsilon_{lv} \end{pmatrix}, \quad (2)$$

where ε_{lh} and ε_{lv} are dielectric eigenvalues of the lth layer in the ordinary and extraordinary directions, respectively. The system is isotropic when $\varepsilon_{lh} = \varepsilon_{lv}$. Here we assume a lossless source layer, i.e., $\varepsilon_s = \mathrm{Re}[\varepsilon_s]$. The subscripts l and s represent variables or constants in the lth and the source layer. The electromagnetic wave can be decomposed into transverse electric (TE) and transverse magnetic (TM) modes (s- and p-polarizations). The dispersion relations for both polarizations are

$$\frac{u_l^2}{\varepsilon_{lh}} + \frac{\kappa^2}{\varepsilon_{lh}} = k_0^2 \quad \text{(TE)}, \qquad \frac{v_l^2}{\varepsilon_{lh}} + \frac{\kappa^2}{\varepsilon_{lv}} = k_0^2 \quad \text{(TM)}, \quad (3)$$

where u_l and v_l are the substrate-normal wave vectors of the TE and TM modes. The dipole source is characterized by an oscillating current with unit strength following

$$\mathbf{J}(\boldsymbol{\xi}) = -i\omega\mathbf{p}_0\delta(\boldsymbol{\xi}), \quad |\mathbf{p_0}| = 1, \qquad \mathbf{E}(\boldsymbol{\xi}) = -i\omega\int \mathbf{G}(\boldsymbol{\xi},\boldsymbol{\xi}')\cdot J(\boldsymbol{\xi}')d^3\boldsymbol{\xi}', \quad (4)$$

where ω is the oscillation frequency, $\mathbf{p}_0$ is the dipole vector, $\mathbf{G}(\xi, \xi')$ is the dyadic Green's function, and $\mathbf{J}(\xi)$ is the current density. To evaluate the time-harmonic electromagnetic wave in a stratified anisotropic structure, we consider the dyadic Green's function of a dipole source embedded in an infinite anisotropic medium as described in Ref. [28]:

$$\mathbf{G}_\infty(\boldsymbol{\xi},\boldsymbol{\xi}') = -\frac{1}{i\omega\varepsilon_0\varepsilon_h}[\nabla\nabla + k_h^2\varepsilon_v\boldsymbol{\varepsilon}^{-1}]\frac{e^{ik_h\xi_e}}{4\pi\xi_e} - i\omega\mu_0\left\{\left(\frac{\varepsilon_v e^{ik_h\xi_e}}{\varepsilon_h 4\pi\xi_e} - \frac{e^{ik_h\xi}}{4\pi\xi}\right)\hat{\boldsymbol{\phi}}\hat{\boldsymbol{\phi}} + \frac{e^{ik_h\xi_e - ik_h\xi}}{4\pi ik_h\rho^2}(\widehat{\boldsymbol{\rho}\boldsymbol{\rho}} - \hat{\boldsymbol{\phi}}\hat{\boldsymbol{\phi}})\right\}, \quad (5)$$

where $\boldsymbol{\varepsilon}_{-1}$ is the inverse dielectric tensor, $k_h^2 \equiv \omega^2\mu_0\varepsilon_0\varepsilon_h$, and $\xi_e^2 = (\varepsilon_v/\varepsilon_h)\rho^2 + z^2$, $\xi^2 = \rho^2 + z^2$. Using the Sommerfeld identity [29], we expand the nonzero electric field components into cylindrical waves:

$$E_{lz}^{\perp} = -\frac{\omega\mu_0 p_0^{\perp}}{4\pi}\frac{\varepsilon_{sh}}{\varepsilon_{sv}}\frac{\varepsilon_{lh}}{\varepsilon_{lv}}\int_0^{\infty}\frac{\kappa^3}{v_s k_{sh} k_{lh}}(f'_{l\perp}e^{iv_l z} + f_{l\perp}e^{-iv_l z} + \delta_{ls}e^{iv_l|z|})J_0(\kappa\rho)d\kappa,$$

$$E_{l\rho}^{\perp} = -\frac{i\omega\mu_0 p_0^{\perp}}{4\pi}\frac{\varepsilon_{sh}}{\varepsilon_{sv}}\int_0^{\infty}\frac{\kappa v_l}{v_s k_{sh} k_{lh}}\left(f'_{l\perp}e^{iv_l z} - f_{l\perp}e^{-iv_l z} + \frac{\delta_{ls}}{\mathrm{sgn}(z)}e^{iv_l|z|}\right)\frac{\partial J_0(\kappa\rho)}{\partial\rho}\,d\kappa,$$

$$E_{lz}^{\parallel} = \frac{i\omega\mu_0 p_0^{\parallel}}{4\pi}\int_0^{\infty}\frac{\kappa^2}{k_{sv}k_{lv}}\left(f'_{l\parallel}\,e^{iv_l z} + f_{l\parallel}e^{-iv_l z} + \frac{\delta_{ls}}{\mathrm{sgn}(z)}e^{iv_l|z|}\right)J_1(\kappa\rho)\cos\phi\ d\kappa,$$

$$E_{l\rho}^{\parallel} = -\frac{\omega\mu_0 p_0^{\parallel}}{4\pi}\int_0^{\infty}\left[\frac{v_l}{k_{sv}k_{lv}}\frac{\varepsilon_{lv}}{\varepsilon_{lh}}(f_{l\parallel}'e^{iv_l z} - f_{l\parallel}e^{-iv_l z} + \delta_{ls}e^{iv_l|z|})\frac{\partial J_1(\kappa\rho)}{\partial\rho}\cos\phi - \frac{1}{u_s}(c'_l e^{iu_l z} + c_l e^{-iu_l z} + \delta_{ls}e^{iu_l|z|})\frac{J_1(\kappa\rho)}{\rho}\cos\phi\right]d\kappa,$$

$$E_{l\phi}^{\parallel} = \frac{\omega\mu_0 p_0^{\parallel}}{4\pi}\int_0^{\infty}\left[\frac{v_l}{k_{sv}k_{lv}}\frac{\varepsilon_{lv}}{\varepsilon_{lh}}(f_{l\parallel}'e^{iv_l z} - f_{l\parallel}e^{-iv_l z} + \delta_{ls}e^{iv_l|z|})\frac{J_1(\kappa\rho)}{\rho}\sin\phi - \frac{1}{u_s}(c'_l e^{iu_l z} + c_l e^{-iu_l z} + \delta_{ls}e^{iu_l|z|})\frac{\partial J_1(\kappa\rho)}{\partial\rho}\sin\phi\right]d\kappa, \tag{6}$$

where $k_{lh}^2 \equiv \omega^2\mu_0\varepsilon_0\varepsilon_{lh}$, $k_{lv}^2 \equiv \omega^2\mu_0\varepsilon_0\varepsilon_{lv}$, $p_0^{\parallel}$ and $p_0^{\perp}$ are the horizontal and vertical dipole moment components, and the source terms are indicated by δ_{ls}. The result becomes identical to the optically isotropic system when $\varepsilon_{lh} = \varepsilon_{lv}$ [24].

The coefficients of the top ($-z$) and bottom ($+z$) traveling eigenfunctions (**M** and **N** in the CPS model [23]), c_l, f_l and c_l', f_l', are determined by the boundary conditions of Maxwell's equations as shown in Fig. S1 within the Supplemental Material [30]. With the coefficients determined, energy transfer into different layers is obtained by calculating the time-averaged divergence of the Poynting vector normalized to the dipole decay rate [23]:

$$b = \frac{e^2 k_s^3}{6\pi m\omega\varepsilon_s}\left[1 + \frac{3q\varepsilon}{2p_0 k_s^3}\mathrm{Im}(E_0)\right] \tag{7}$$

or

$$\frac{b}{b_0} = 1 - q + q\left\{1 + \frac{\mathrm{Im}[\mathbf{p}\cdot\mathbf{E}(\boldsymbol{\xi}')]}{\mathrm{Im}[\mathbf{p}\cdot\mathbf{E}_\infty(\boldsymbol{\xi}')]}\right\}, \tag{8}$$

where $b(b_0)$ is the exciton decay rate in an optical cavity (free space), $\mathbf{E}_\infty(\boldsymbol{\xi}')$ is the electric field with a dipole embedded in an infinite anisotropic source layer in free space, $\mathbf{E}(\boldsymbol{\xi}')$ is the electric field with a dipole embedded in a source layer that is in a stratified cavity structure, and q is the radiative quantum yield. Birefringence is calculated by expressing b separately for substrate-parallel and normal orientations. The total decay rate is obtained by the weighted average of the two decay rates:

$$b_{\mathrm{tot}} = \theta_{\mathrm{hor}}\cdot b_{\parallel} + (1 - \theta_{\mathrm{hor}})b_{\perp}, \tag{9}$$

where θ_{hor} is the ratio of horizontal-to-vertically aligned TDMs defined as

$$\theta_{\mathrm{hor}} = \frac{\mathrm{TM}_{||} + \mathrm{TE}_{||}}{\mathrm{TM}_{\perp} + \mathrm{TM}_{||} + \mathrm{TE}_{||}}. \tag{10}$$

Thus, θ_{hor}= 67% for random alignment ($\mathrm{TM}_{\perp}$= $\mathrm{TM}_{\parallel}$= $\mathrm{TE}_{\parallel}$) and θ_{hor}= 100% for all TDMs oriented parallel to the substrate. Next, we calculate the divergence of the normalized Poynting vector. Assuming the structure is infinite in the x-y plane, we get [24]

$$\int\nabla\cdot\mathbf{S}\,\mathrm{dV} \approx \oint\mathbf{S}\cdot\hat{\mathbf{z}}d\sigma = \mathrm{S}_z^{+} - \mathrm{S}_z^{-},$$

$$S_z = \frac{i}{2\mu_0\omega}\left[E_\rho\left(\frac{\partial E_\rho}{\partial z} - \frac{\partial E_z}{\partial\rho}\right)^{*} + E_\phi\left(\frac{\partial E_\phi}{\partial z} - \frac{\partial E_z}{\rho\partial\phi}\right)^{*}\right], \tag{11}$$

where the superscripts + and − denote the forward-propagating ($+z$) and backward-propagating ($-z$) energy flux through the bottom and top interfaces of the lth layer, respectively. Defining $k_\rho = \kappa/k_{sh}$ as the normalized surface-parallel wave vector, we calculate the normalized perpendicular components of the Poynting vector by inserting the electric field into Eq. (11). Integrating over x-y and applying the Bessel function closure relation, we get

$$\mathrm{Re}[S_{l,z}^{\perp}(k_\rho)] = \frac{3q}{4}\left|\frac{\varepsilon_{sh}}{\varepsilon_{sv}}\right|^2\mathrm{Re}\left\{\sqrt{\frac{\varepsilon_{lh}^*}{\varepsilon_{lv}}}\frac{{k_\rho}^3\sqrt{\varepsilon_{lv}/\varepsilon_{sh} - {k_\rho}^2}}{|1 - \varepsilon_{sh}/\varepsilon_{sv}\cdot{k_\rho}^2|}(f'_{l\perp}e^{iv_l z_{0l}} - f_{l\perp}e^{-iv_l z_{0l}})\times(f'_{l\perp}e^{iv_l z_{0l}} + f_{l\perp}e^{-iv_l z_{0l}})^{*}\right\},$$

$$\mathrm{Re}[S_{l,z}^{\parallel}(k_\rho)] = \frac{3q\varepsilon_{sh}}{2(3\varepsilon_{sh} + \varepsilon_{sv})}\mathrm{Re}\left\{\frac{\varepsilon_{sh}}{\varepsilon_{sv}}\sqrt{\frac{\varepsilon_{lh}^*}{\varepsilon_{lv}}}\left[k_\rho\sqrt{\frac{\varepsilon_{lv}}{\varepsilon_{sh}} - {k_\rho}^2}(f'_{l\parallel}e^{iv_l z_{0l}} - f_{l\parallel}e^{-iv_l z_{0l}})(f'_{l\perp}e^{-iv_l z_{0l}} + f_{l\perp}e^{iv_l z_{0l}})^{*}\right.\right.$$
$$\left.\left. + \frac{k_\rho\sqrt{\varepsilon_{lh}/\varepsilon_{sh} - {k_\rho}^2}^{*}}{|1 - {k_\rho}^2|}(c'_l e^{iu_l z_{0l}} + c_l e^{-iu_l z_{0l}})(c'_l e^{iu_l z_{0l}} - c_l e^{-iu_l z_{0l}})^{*}\right]\right\}, \tag{12}$$

which becomes identical to the result in an isotropic medium when $\varepsilon_{lh} = \varepsilon_{lv}$ [24].

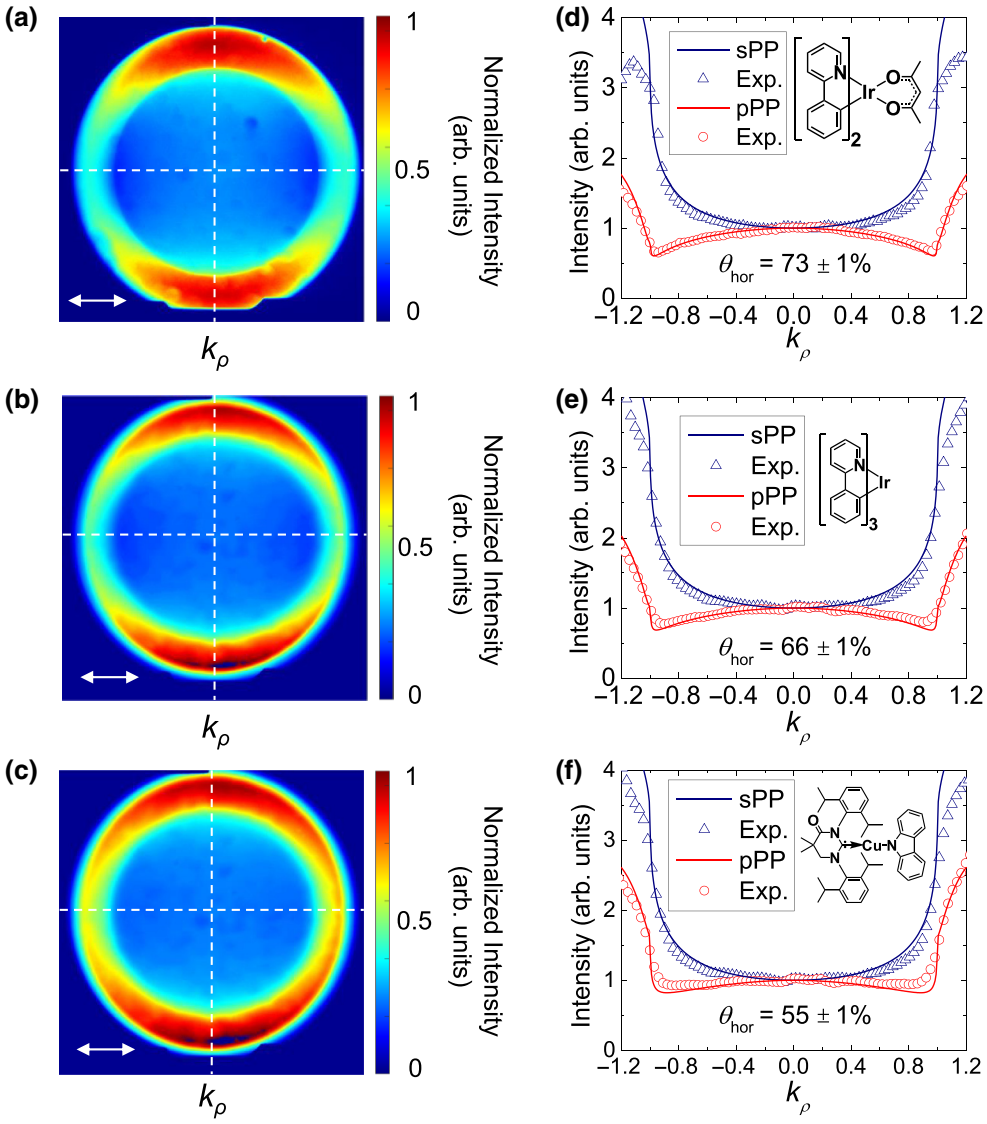

FIG. 2. Measured polar plots (a)–(c) and intensity profiles in the pPP and sPP (d)–(f) (data points) along with simulated fits (solid lines) for $Irppy_2(acac)$ (a),(d), $Irppy_3$ (b),(e), and (MAC)CuCz (c),(f) doped at 10 vol. % into a CBP host. Insets: molecular structural formulae of dopants.

Then,

$$F_{0,\perp}(k_\rho) = \frac{n_{\text{glass}}}{n_{sv}k_\rho}\text{Re}[S^{\perp}_{N,z}(k_\rho)],$$
$$F_{0,\parallel}(k_\rho) = \frac{n_{\text{glass}}}{n_{sh}k_\rho}\text{Re}[S^{\parallel}_{N,z}(k_\rho)], \quad (13)$$

where $F_{0,\perp}$ and $F_{0,||}$ correspond to the field intensity for substrate-normal ($\perp$) and substrate-parallel ($\parallel$) dipoles, which correspond to the Fourier transform of the input photoluminescence as previously shown in Eq. (1). Unlike the angular spectrum of a point source that has a tangential relationship (u/k_ρ or v/k_ρ) between the Poynting vector and the field intensity, $1/k_\rho$ appears in Eq. (13). This difference stems from the detection of FIM using a planar CCD, where Lambert's cosine law does not apply. The fraction of energy transferred from the source to each layer is obtained by integrating $\text{Re}[S_{l,z}(k_\rho)]$ for all k_ρ and then dividing by the corresponding decay rate b/b_0.

The lens projects a polar plot in the back focal plane with an angle of in-plane rotation, φ, as shown in Fig. 1(d). Molecules deposited during layer growth often lack a rotational preference. Thus, the output intensity distribution in the focal plane shows an in-plane symmetry. Placing a linear polarizer in front of the back focal plane breaks the symmetry, leading to an improved fitting accuracy of the polar intensity information to Eq. (13). Then we define two orthogonal planes, one parallel [blue plane, Fig. 1(d)] and the other perpendicular (red plane) to the polarizer, defined as *p*-polarized (pPP) and *s*-polarized (sPP) dipole planes, respectively. As shown in Fig. 1(d), pPP includes vertically and horizontally aligned TDMs relative to the substrate, whereas sPP includes only one horizontally aligned TDM. The projected *k*-space image in the back focal plane then follows the cosine square law

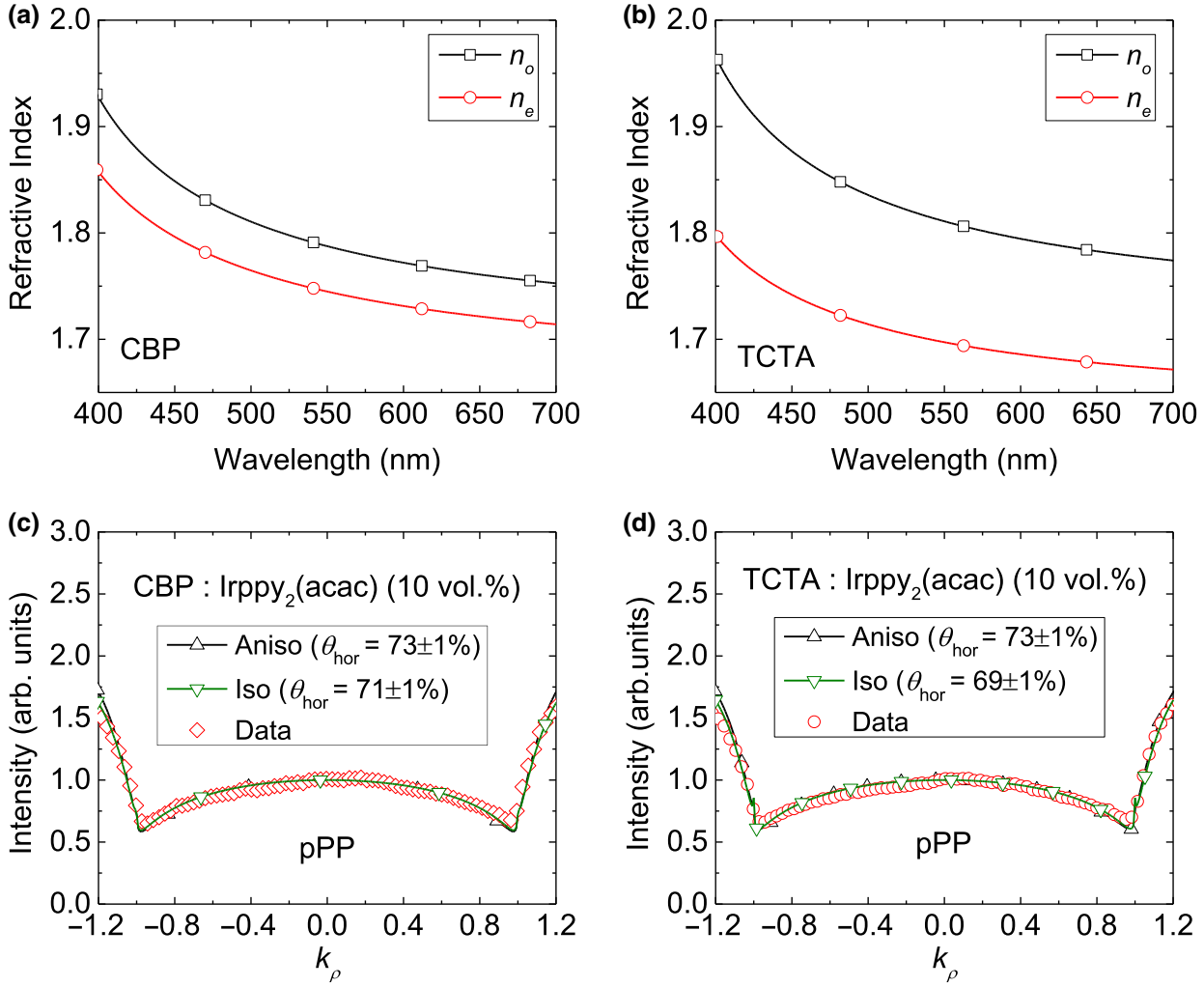

FIG. 3. Transition dipole orientation measurement in a birefringent host matrix. Refractive index of (a) CBP and (b) TCTA. Here n_o and n_e are the indexes of refraction along the ordinary and extraordinary optical axes, respectively. Measured intensity profiles of Irppy$_2$(acac) doped in (c) CBP and (d) TCTA at 10 vol. %. Note that there is an error in the orientation measurement of 2% for CBP and 4% in TCTA with its larger birefringence.

of a linear polarizer:

$$U_f(r,\varphi) = \frac{1}{i\lambda f}\{[(1-\theta_{\rm hor})F_{0,\perp,\,\rm pPP}(k_\rho) + \theta_{\rm hor}F_{0,\,||,\,\rm pPP}(k_\rho)]\cos^2\varphi + [\theta_{\rm hor}F_{0,\,||,\,\rm sPP}(k_\rho)]\sin^2\varphi\}. \quad (14)$$

III. EXPERIMENT

Films for FIM measurement are grown on precleaned 0.2-mm-thick fused silica substrates by vacuum thermal evaporation (VTE) in a chamber with a base pressure of 1×10^{-7} torr. The deposition rates of the molecules are adjusted to achieve the desired dopant concentrations in the host, and the film thicknesses are controlled using quartz crystal thickness monitors. We deposit a 50-nm-thick Al marker on the samples to precisely focus the microscope on the film on the front focal plane. Following the deposition, devices are encapsulated using an epoxy seal around the edge of a cover glass in a N_2 environment.

The Fourier microscope consists of two parts: (i) an inverted fluorescence microscope comprising a 325-nm He-Cd continuous-wave laser with an inverted microscope (Olympus IX73) and (ii) a system of optical components comprising a Fourier lens (Thorlabs), optical filters, a linear polarizer, and a spectrometer with a 1024×1024 CCD array (Princeton Instruments). The photoluminescence of the sample is coupled through an oil immersion objective ($\times100$, NA = 1.40, Olympus). The Fourier lens (f = 300 mm) reconstructs the Fourier image plane on the CCD. A long-pass filter is used to prevent the reflected laser beam from being incident on the CCD, while a filter

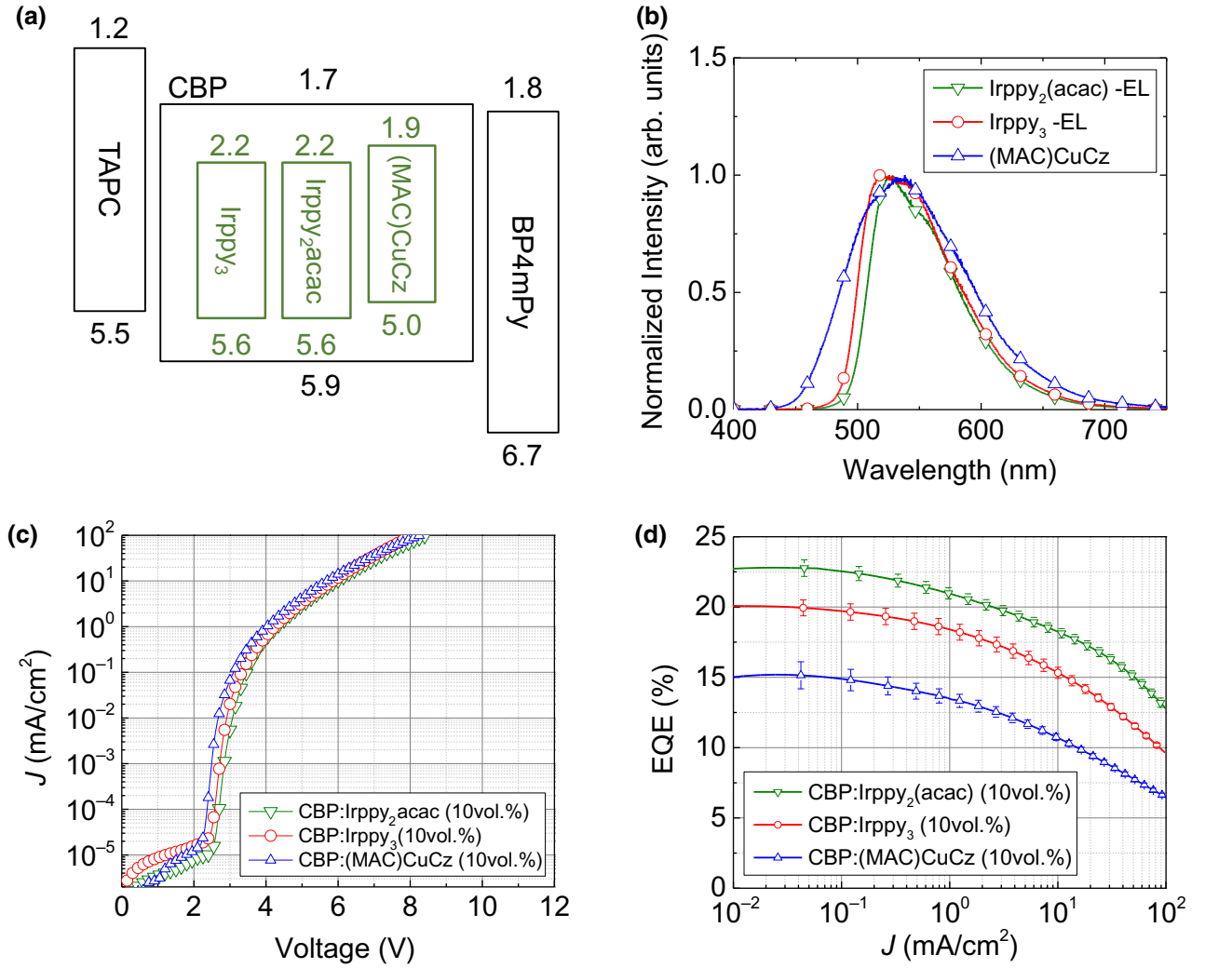

FIG. 4. Performance of OLEDs with the three dopant emitting molecules in Fig. 2. (a) Frontier orbital energies of the materials in eV. The electroluminescence spectra (b), current density–voltage (J-V) characteristics (c), and the current density versus external quantum efficiency (J-η_{EQE}) characteristics (d) of the OLEDs.

with a pass band near the peak wavelength of the dopant photoluminescence is also placed in the optical path. A linear polarizer separates the emission into two orthogonal planes corresponding to the pPP and sPP modes. To suppress imaging artifacts in the high-k region, the k-space fitting in pPP is performed over a limited range of $-1.1 < k_x/k_0 < 1.1$ [12–14,21,31].

OLEDs are grown on 1-mm-thick cleaned glass substrates with a predeposited, patterned 150-nm-thick ITO layer (Thin Film Devices, Inc.). Prior to film deposition by VTE, the ITO-coated substrates are treated in a UV-ozone chamber for 15 min. CBP, $Irppy_2(acac)$, $Irppy_3$, 1,1-bis[(di-4-tolylamino)phenyl]cyclohexane (TAPC), and 3,3′,5,5′-tetra[(M-pyridyl)-phen-3-yl]biphenyl (BP4mPy) are purchased from Luminescence Technology, Corp. The device area of 2 mm^2 is defined by the intersection of a prepatterned 1-mm-wide ITO strip and an orthogonal 2-mm-wide Al cathode strip patterned by deposition through a metal shadow mask. The current density–voltage (J-V) characteristics are measured using a parameter analyzer (HP4145, Hewlett-Packard) and a calibrated photodiode (FDS1010-CAL, Thorlabs) following standard procedures [32]. The emission spectra at $J = 100$ mA/cm^2 are recorded using a calibrated spectrometer (USB4000, Ocean Optics) coupled to the device with an optical fiber.

IV. RESULTS

Figures 2(a)–2(c) show measured intensity patterns for thin films comprising $Irppy_2(acac)$, $Irppy_3$ and (MAC)CuCz doped at 10 vol. % into a CBP host matrix. The measured pPP and sPP intensity profiles compared with the simulation fits in Figs. 2(d)–2(f) show a horizontal and isotropic orientation of the TDM with respect to

the substrate from $Irppy_2(acac)$ and $Irppy_3$ doped in CBP ($\theta_{hor} = 73 \pm 1\%$ and $66 \pm 1\%$), respectively, which are consistent with previous measurements [33–35], whereas (MAC)CuCz in CBP shows a relatively vertically aligned TDM ($\theta_{hor} = 55 \pm 1\%$) as shown in Fig. 2(f).

The results for $Irppy_2(acac)$ doped in a birefringent host, tris(4-carbazoyl-9-ylphenyl)amine (TCTA), are depicted in Fig. 3 to show the effect of an anisotropic medium on the emission. The measured refractive index of CBP and TCTA is shown in Figs. 3(a) and 3(b), demonstrating a larger birefringence of TCTA. The FIM intensity patterns in pPP for CBP and TCTA hosts are shown in Figs. 3(c) and 3(d). Two different fit results based on isotropic and anisotropic media are used to compare each measurement, showing an increased discrepancy when assuming an anisotropic dielectric constant for TCTA compared to the CBP host matrix.

OLEDs comprising these dopants are fabricated with the following structures: Al 100 nm/8-quinolinolatolithium (LiQ) 1.5 nm/BP4mPy 50 nm/CBP:Dopant (10 vol. %) 15 nm/TAPC 40 nm/MoO_3 2 nm/ITO 150 nm. Figure 4(a) shows the frontier orbital energies for the OLEDs, and Fig. 4(b) shows the corresponding OLED electroluminescent spectra. The J-V characteristics of the devices in Fig. 4(c) show negligible differences due to the identical device structures. The peak external quantum efficiency (EQE) in Fig. 4(d) is approximately 1.5 times higher for $Irppy_2(acac)$ than (MAC)CuCz.

In Fig. 5, the simulated coupling efficiency of each mode as a function of θ_{hor} at 530 nm is compared with the measured peak EQE of the OLEDs (data points). Here, the simulated fraction of the emitted light power coupled into each mode is shown along the vertical axis. The fraction of air and substrate mode coupling increases with θ_{hor}, whereas coupling to surface plasmon polaritons (SP) decreases.

V. DISCUSSION

The external quantum efficiency of an OLED is given by

$$\eta_{EQE} = \eta_{int}\eta_{out} = \gamma\chi_{ST}\eta_{PL}\eta_{out}, \tag{15}$$

where η_{int} is the internal quantum efficiency, which is the ratio of the number of photons generated to the number of injected charges. The internal quantum efficiency is the product of the charge balance factor (γ), spin formation ratio (χ_{ST}), and photoluminescence quantum yield (η_{PL}). The value of χ_{ST} is 100% for electrophosphorescent (PHOLED) and thermally assisted delayed fluorescent (TADF) devices. Also, η_{out} is the outcoupling efficiency, which is the fraction of photons coupled into air modes versus the total number of photons generated.

The Ir-based PHOLEDs and the (MAC)CuCz TADF OLEDs in Fig. 4 have identical device structures. The

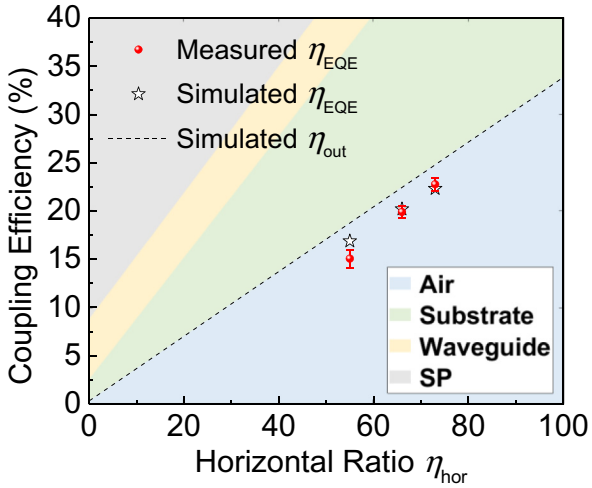

FIG. 5. Calculated distribution of the emitted power into different modes depending on the average orientation of the transition dipole moment within the emissive layer. The data points show the measured and simulated η_{EQE} of the OLEDs comprising different dopant emitters. The simulated points are based on FIM measurements of the dopant molecule orientations relative to the substrate. The color bands indicate the proportion of light power coupled into each mode.

J-V characteristics in Fig. 4(c) show no noticeable differences since the energy levels of all dopants are nested in the host matrix energy gap, thus experiencing similar charge transfer efficiencies from host to dopant. Therefore, we conclude that the three devices have similar γ. Also, $\eta_{PL} > 90\%$ for all three molecules [33,36,37], leading to nearly identical η_{int}. However, the EQE in Fig. 4(d) shows noticeable differences from device to device, reaching approximately 1.5 times higher for the $Irppy_2(acac)$ device compared to the (MAC)CuCz OLED.

From the above, the relative differences of EQE between the dopant molecules can, therefore, be attributed to differences in outcoupling efficiency resulting from variations in TDM orientation. The coupling into different modes as a function of TDM orientation is simulated in Fig. 5. The vertical TDM emits TM polarized light primarily in the substrate-parallel direction. Therefore, the majority of power from the vertical TDM is coupled to either SP modes, or waveguide and substrate modes, depending on the electron transport layer (ETL) thickness that determines the distance between the metal cathode and the emitting dipoles. A thin ETL results in a larger fraction of power being coupled to SP modes due to near-field coupling. Consequently, the fraction of light coupled into air modes decreases with an increasing fraction of vertically oriented TDMs as shown in Fig. 5. The simulation shows peak outcoupling efficiencies of 24.8%, 22.4%, and 18.7% for OLEDs with $\theta_{hor} = 73\%$, 66%, and 55%, respectively. Assuming $\gamma = \chi_{ST} = 100\%$ and $\eta_{PL} = 90\%$ for the three dopant molecules [33,36,37], the simulated $\eta_{EQE} = 22.3\%$,

20.2%, and 16.9%, which correspond to the experimental result, $\eta_{EQE} = 22.8 \pm 0.7\%$, $19.2 \pm 0.6\%$, and $15.1 \pm 0.9\%$.

The most commonly used alternative methods for measuring molecular orientation are variable-angle spectral ellipsometry (VASE), grazing incidence wide-angle x-ray diffraction (GIWAXD), and angle-dependent photoluminescence spectral measurements (Angle PL) [9–11]. Despite their simplicity and precision, VASE and GIWAXD do not have the sensitivity to resolve the alignment of the dopant emitters in dilute thin films. On the other hand, Angle PL overcomes this problem by directly measuring the emitting dopant orientation. However, Angle PL suffers from the need for precise alignment of optical components, and a slow rate of data acquisition along only a single axis. Since Angle PL requires rotational movement, with distance from the detector to the sample on the scale of the lens focal length, a small tilt or shift of the sample holder causes significant measurement inaccuracies. On the other hand, FIM simultaneously measures the radiation at all angles, providing a simple and precise measurement of the TDM orientation in real time [13,14,25].

VI. CONCLUSIONS

We combine the CPS dipole model with Fourier optics to describe the far-field radiation distribution pattern in the back focal plane of a converging lens originating from a light-emitting point dipole within a stratified birefringent thin film. By comparing the measured emission pattern using Fourier imaging microscopy with simulations, we determine the average orientation of the transition-dipole-moment vectors within an organic film. We apply this technique to measure the TDM orientations of three different molecules, namely $Irppy_2(acac)$, $Irppy_3$, and (MAC)CuCz doped into a CBP host matrix. The OLED outcoupling efficiencies agree to within experimental error with that obtained using FIM. This technique can be used to understand and optimize light outcoupling in a variety of materials systems and device structures.

ACKNOWLEDGMENTS

The work is supported by the U.S. Department of Energy, Office of Basic Energy Sciences, Award No. DE-SC0017971 (theory, data analysis, experimental details) and Universal Display Corporation (OLED engineering).

[1] P. Sullivan, T. S. Jones, A. J. Ferguson, and S. Heutz, Structural templating as a route to improved photovoltaic performance in copper phthalocyanine/fullerene (C60) heterojunctions, Appl. Phys. Lett. **91**, 233114 (2007).

[2] D. Chen, A. Nakahara, D. Wei, D. Nordlund, and T. P. Russell, P3HT/PCBM bulk heterojunction organic photovoltaics: Correlating efficiency and morphology, Nano Lett. **11**, 561 (2011).

[3] Y. Watanabe, H. Sasabe, and J. Kido, Review of molecular engineering for horizontal molecular orientation in organic light-emitting devices, Bull. Chem. Soc. Jpn. **92**, 716 (2019).

[4] T. D. Schmidt, T. Lampe, D. Sylvinson M. R., P. I. Djurovich, M. E. Thompson, and W. Brütting, Emitter Orientation as a Key Parameter in Organic Light-Emitting Diodes, Phys. Rev. Appl. **8**, 037001 (2017).

[5] S. Y. Byeon, J. Kim, D. R. Lee, S. H. Han, S. R. Forrest, and J. Y. Lee, Nearly 100% horizontal dipole orientation and upconversion efficiency in blue thermally activated delayed fluorescent emitters, Adv. Opt. Mater. **6**, 1701340 (2018).

[6] D. Yokoyama, Y. Setoguchi, A. Sakaguchi, M. Suzuki, and C. Adachi, Orientation control of linear-shaped molecules in vacuum-deposited organic amorphous films and its effect on carrier mobilities, Adv. Funct. Mater. **20**, 386 (2010).

[7] G. R. Mitchell, A wide-angle X-Ray study of the development of molecular orientation in crosslinked natural rubber, Polymer **25**, 1562 (1984).

[8] J. Als-Nielsen, D. Jacquemain, K. Kjaer, F. Leveiller, M. Lahav, and L. Leiserowitz, Principles and applications of grazing incidence X-Ray and neutron scattering from ordered molecular monolayers at the air-water interface, Phys. Rep. **246**, 251 (1994).

[9] J. Frischeisen, D. Yokoyama, C. Adachi, and W. Brütting, Determination of molecular dipole orientation in doped fluorescent organic thin films by photoluminescence measurements, Appl. Phys. Lett. **96**, 073302 (2010).

[10] S. Nowy, B. C. Krummacher, J. Frischeisen, N. A. Reinke, and W. Brütting, Light extraction and optical loss mechanisms in organic light-emitting diodes: Influence of the emitter quantum efficiency, J. Appl. Phys. **104**, 123109 (2008).

[11] C.-K. Moon, S.-Y. Kim, J.-H. Lee, and J.-J. Kim, Luminescence from oriented emitting dipoles in a birefringent medium, Opt. Express **23**, A279 (2015).

[12] M. A. Lieb, J. M. Zavislan, and L. Novotny, Single-molecule orientations determined by direct emission pattern imaging, J. Opt. Soc. Am. B **21**, 1210 (2004).

[13] J. A. Schuller, S. Karaveli, T. Schiros, K. He, S. Yang, I. Kymissis, J. Shan, and R. Zia, Orientation of luminescent excitons in layered nanomaterials, Nat. Nanotechnol. **8**, 271 (2013).

[14] M. Böhmler, N. Hartmann, C. Georgi, F. Hennrich, A. A. Green, M. C. Hersam, and A. Hartschuh, Enhancing and redirecting carbon nanotube photoluminescence by an optical antenna, Opt. Express **18**, 16443 (2010).

[15] S. J. Brown, R. A. DeCrescent, D. M. Nakazono, S. H. Willenson, N. A. Ran, X. Liu, G. C. Bazan, T.-Q. Nguyen, and J. A. Schuller, Enhancing organic semiconductor–surface plasmon polariton coupling with molecular orientation, Nano Lett. **17**, 6151 (2017).

[16] S. J. Brown, R. A. Schlitz, M. L. Chabinyc, and J. A. Schuller, Morphology-dependent optical anisotropies in the n -type polymer P(NDI2OD-T2), Phys. Rev. B **94**, 165105 (2016).

[17] A. Fieramosca, L. De Marco, M. Passoni, L. Polimeno, A. Rizzo, B. L. T. Rosa, G. Cruciani, L. Dominici, M. De Giorgi, G. Gigli, L. C. Andreani, D. Gerace, D. Ballarini, and D. Sanvitto, Tunable out-of-plane excitons in 2D single-crystal perovskites, ACS Photonics **5**, 4179 (2018).

[18] Y. Gao, M. C. Weidman, and W. A. Tisdale, Cdse nanoplatelet films with controlled orientation of their transition dipole moment, Nano Lett. **17**, 3837 (2017).

[19] M. J. Jurow, T. Morgenstern, C. Eisler, J. Kang, E. Penzo, M. Do, M. Engelmayer, W. T. Osowiecki, Y. Bekenstein, C. Tassone, L.-W. Wang, A. P. Alivisatos, W. Brütting, and Y. Liu, Manipulating the transition dipole moment of $CsPbBr_3$ perovskite nanocrystals for superior optical properties, Nano Lett. **19**, 2489 (2019).

[20] D. Pommier, R. Bretel, L. E. P. López, F. Fabre, A. Mayne, E. Boer-Duchemin, G. Dujardin, G. Schull, S. Berciaud, and E. Le Moal, Scanning Tunneling Microscope-Induced Excitonic Luminescence of a Two-Dimensional Semiconductor, Phys. Rev. Lett. **123**, 027402 (2019).

[21] T. H. Taminiau, F. D. Stefani, F. B. Segerink, and N. F. van Hulst, Optical antennas direct single-molecule emission, Nat. Photonics **2**, 234 (2008).

[22] T. H. Taminiau, S. Karaveli, N. F. van Hulst, and R. Zia, Quantifying the magnetic nature of light emission, Nat. Commun. **3**, 979 (2012).

[23] R. R. Chance, A. Prock, and R. Silbey, Lifetime of an emitting molecule near a partially reflecting surface, J. Chem. Phys. **60**, 2744 (1974).

[24] K. Celebi, T. D. Heidel, and M. A. Baldo, Simplified calculation of dipole energy transport in a multilayer stack using dyadic Green's functions, Opt. Express **15**, 1762 (2007).

[25] J. W. Goodman, *Introduction to Fourier Optics*, 2nd ed (McGraw Hill, New York, 1996).

[26] L. Penninck, P. De Visschere, J. Beeckman, and K. Neyts, Dipole radiation within one-dimensional anisotropic microcavities: A simulation method, Opt. Express **19**, 18558 (2011).

[27] M. K. Callens, D. Yokoyama, and K. Neyts, Anisotropic materials in OLEDs for high outcoupling efficiency, Opt. Express **23**, 21128 (2015).

[28] W. S. Weiglhofer, Dyadic Green's functions for general uniaxial media, IEE Proc. H Microw. Antennas Propag. **137**, 5 (1990).

[29] Z. Xiong, Electromagnetic fields of electric dipoles embedded in a stratified anisotropic earth, Geophysics **54**, 1643 (1989).

[30] See Supplemental Material at http://link.aps.org/supplemental/10.1103/PhysRevApplied.14.034048 for detailed boundary conditions and data analysis.

[31] J. A. Kurvits, M. Jiang, and R. Zia, Comparative analysis of imaging configurations and objectives for Fourier microscopy, J. Opt. Soc. Am. A **32**, 2082 (2015).

[32] S. R. Forrest, D. D. C. Bradley, and M. E. Thompson, Measuring the efficiency of organic light-emitting devices, Adv. Mater. **15**, 1043 (2003).

[33] P. Liehm, C. Murawski, M. Furno, B. Lüssem, K. Leo, and M. C. Gather, Comparing the emissive dipole orientation of two similar phosphorescent green emitter molecules in highly efficient organic light-emitting diodes, Appl. Phys. Lett. **101**, 253304 (2012).

[34] C. Mayr and W. Brütting, Control of molecular dye orientation in organic luminescent films by the glass transition temperature of the host material, Chem. Mater. **27**, 2759 (2015).

[35] A. Graf, P. Liehm, C. Murawski, S. Hofmann, K. Leo, and M. C. Gather, Correlating the transition dipole moment orientation of phosphorescent emitter molecules in OLEDs with basic material properties, J. Mater. Chem. C **2**, 10298 (2014).

[36] S. Shi, M. C. Jung, C. Coburn, A. Tadle, M. R. D. Sylvinson, P. I. Djurovich, S. R. Forrest, and M. E. Thompson, Highly efficient photo- and electroluminescence from two-coordinate Cu(I) complexes featuring nonconventional N-heterocyclic carbenes, J. Am. Chem. Soc. **141**, 3576 (2019).

[37] Y. Kawamura, K. Goushi, J. Brooks, J. J. Brown, H. Sasabe, and C. Adachi, 100% phosphorescence quantum efficiency of Ir(III) complexes in organic semiconductor films, Appl. Phys. Lett. **86**, 071104 (2005).